An increase in dendritic plateau potentials is associated with experience-dependent cortical map reorganization

Stéphane Pagès[a,1] [ID], Nicolas Chenouard[b,1], Ronan Chéreau[a] [ID], Vladimir Kouskoff[b], Frédéric Gambino[b,2,3] [ID], and Anthony Holtmaat[a,2,3]

[a]Department of Basic Neurosciences and the Center for Neuroscience, Centre Médical Universitaire (CMU), University of Geneva, 1211 Geneva, Switzerland; and [b]University of Bordeaux, CNRS, Interdisciplinary Institute for Neuroscience, UMR 5297, F-33000 Bordeaux, France

The organization of sensory maps in the cerebral cortex depends on experience, which drives homeostatic and long-term synaptic plasticity of cortico-cortical circuits. In the mouse primary somato-sensory cortex (S1) afferents from the higher-order, posterior medial thalamic nucleus (POm) gate synaptic plasticity in layer (L) 2/3 pyramidal neurons via disinhibition and the production of dendritic plateau potentials. Here we address whether these thalamo-cortically mediated responses play a role in whisker map plasticity in S1. We find that trimming all but two whiskers causes a partial fusion of the representations of the two spared whiskers, concomitantly with an increase in the occurrence of POm-driven N-methyl-D-aspartate receptor-dependent plateau potentials. Blocking the plateau potentials restores the archetypical organization of the sensory map. Our results reveal a mechanism for experience-dependent cortical map plasticity in which higher-order thalamocortically mediated plateau potentials facilitate the fusion of normally segregated cortical representations.

synaptic plasticity | dendritic signaling | posterior medial complex of the thalamus | somatosensory | barrel cortex

Sensory cortices contain functional topographic maps, which can rapidly change in response to training and altered sensory experience (1). For example, whisker trimming in rodents modifies the proportional representation of spared and trimmed whiskers in the barrel field of the primary sensory cortex (S1) (1–4). This type of cortical map plasticity is thought to be driven by long-term potentiation (LTP) and long-term depression (LTD) of layer (L) 4-to-L2/3 and L2/3-L2/3 cortico-cortical (CC) synapses (2, 5–7), as well as by changes in intrinsic neuronal properties and homeostatic mechanisms balancing the loss of surrounding sensory inputs (8, 9). In addition, whisker trimming weakens feed-forward inhibition of L2/3 pyramidal neurons (10–12), and, similarly to monocular deprivation, even may evoke pruning of inhibitory synapses (13–15). Disinhibition could also serve a role in homeostasis by increasing whisker-evoked neuronal spiking (9) and gate synaptic plasticity (12).

Thalamo-cortical (TC) synapses may play a direct or facilitating role in cortical map plasticity. TC axons have been shown to remain plastic throughout life and to be affected by modifications of sensory experience (16–19). Trimming a subset of whiskers causes a decrease in TC innervation of deprived but not of spared barrels (16, 18), and sensory learning may induce plasticity of a subset of TC synapses (20). However, the relative contributions of CC and TC synaptic plasticities, and how they interact during cortical map plasticity, is not known. Moreover, the role of TC synapses may be intricate since different cortical layers receive inputs from diverse thalamic origins, each with distinctive properties.

Sensory information from the whiskers is transmitted to S1 by two main and well-segregated TC projections (21–23). The lemniscal pathway relays sensory information to L5b, L4, and L3 neurons through the ventral posteromedial (VPM) nucleus of

the thalamus (22). The paralemniscal pathway provides a complementary and nonoverlapping source of inputs mainly terminating in L5a and L1 that arise from the higher-order posterior medial thalamic nucleus (POm) of the thalamus. While the VPM is viewed as the main hub for whisker tactile information to S1, the exact function of the POm in this cortical area remains unclear (24, 25). Neurons in the POm have broad receptive fields (26, 27), and their axons have extensive arborizations in S1, distributed over multiple barrel-related columns (22, 28, 29). POm axons connect to distal pyramidal cell dendrites as well as to various interneurons (20, 30–35). The large extent of their projections together with their broad receptive fields suggests that POm neurons provide more global input to S1 as compared to VPM neurons.

POm projections to S1 mediate whisker-evoked N-methyl-D-aspartate receptor (NMDAR)-dependent plateau potentials and facilitate whisker-evoked LTP in L2/3 pyramidal neurons (36), which may depend on a combined excitation and disinhibition (34). In addition, POm projections themselves display plasticity during sensory learning (20). Altogether, this suggests that POm projections to S1 could play a distinctive role in the

---

Significance

Here we describe a mechanism for cortical map plasticity. Classically, representational map changes are thought to be driven by changes within cortico-cortical circuits, e.g., Hebbian plasticity of synaptic circuits that lost vs. maintained an excitatory drive from the first-order thalamus, possibly steered by neuromodulatory forces from deep brain regions. Our work provides evidence for an additional gating mechanism, provided by plateau potentials, which are driven by higher-order thalamic feedback. Higher-order thalamic neurons are characterized by broad receptive fields, and the plateau potentials that they evoke strongly facilitate long-term potentiation and elicit spikes. We show that these features combined constitute a powerful driving force for the fusion or expansion of sensory representations within cortical maps.

NEUROSCIENCE

refinement of cortical maps. Here, we investigate the relationship between cortical remapping and POm-mediated plateau potentials upon whisker sensory deprivation. We use a paradigm in which all whiskers were trimmed except a pair of neighboring ones (dual-whisker experience, DWE). Using intrinsic optical imaging, we first corroborate previous electrophysiology studies which showed that DWE causes the representation of the two spared whiskers to partly fuse (37, 38). We then show that this plasticity is associated with an increase in dendritic plateau potentials, which is dependent on inputs from the POm. The pharmacological removal of the plateau potentials causes the fused whisker representations to segregate back to an organization seen in naive mice. Altogether, our results reveal a mechanism for rapid experience-dependent cortical map plasticity, which consists of an increased contribution of dendritic plateau potentials that are associated with inputs from higher-order thalamic neurons. This, in turn, may enhance the level of non-specific sensory input and facilitate subsequent synaptic plasticity events that have been shown to underlie cortical map reorganization (2–4, 6).

Results

Dual-Whisker Experience Reshapes Whisker-Evoked Intrinsic Optical Signals in S1. Single-unit and whole-cell recordings have shown that DWE causes the functional representation of the spared whiskers in S1 to merge (4, 12, 37, 38). Intrinsic optical signal (IOS) imaging, which is a proxy of whisker-evoked population activity (39, 40), can potentially quantify such changes at the mesoscale level in a quasi-noninvasive manner (41–43). Here, we used IOS imaging to measure DWE-evoked plasticity of whisker representations in S1.

Mice were separated in two groups. One group was exposed to a brief period of DWE (1 to 4 d) by clipping all whiskers except whisker C1 and C2, while for the control group all whiskers were left intact to allow a full whisker experience (FWE). We used IOS to assess the spatial representation of the C1 and C2 whiskers in S1 under urethane anesthesia (Fig. 1A). In FWE mice, the whiskers other than C1 and C2 were trimmed under anesthesia, just prior to imaging, to create similar stimulus conditions as in DWE mice (DWE 0 in Fig. 1). For each mouse, 100-ms-long imaging frames were acquired through the skull before (frames 1 to 10), during (frames 11 to 20), and after (frames 21 to 50) a 1-s long train (8 Hz) of single whisker deflections (Fig. 1A). The whisker-evoked response area and the corresponding center were then computed by a statistical comparison of the averaged baseline (frames 1 to 10) and whisker-evoked (frames 19 to 28) IOS over at least 10 successive trials. This was done by using a pixel-by-pixel paired t test as previously described (43). For each whisker, the resulting t-value map was low-pass-filtered with a Gaussian kernel (200 μm full width at half maximum) and thresholded (t-value threshold = −2). Only pixels with a t-value below the threshold were included into the stimulus-evoked response area (Fig. 1B). The peak of the response area was given by the minimum in the t-value distribution. The Euclidian distance between the peaks of the C1 and C2 response areas was used to determine the distance between the two whisker representations (hereafter termed whisker representation distance [WRD]) as a function of time after deprivation (43) (Fig. 1 B–D).

We found that, while the WRD was similar after 1 d of DWE as compared to FWE (DWE$_0$: 266 ± 3.7 μm, $n = 31$; DWE$_1$: 255 ± 13 μm, $n = 9$; $P = 0.455$), it was significantly decreased after 2 d of DWE (DWE$_0$: 266 ± 3.7 μm, $n = 31$; DWE$_2$: 214 ± 16 μm, $n = 8$; $P = 0.01$) (Fig. 1C). This indicates that DWE narrows the distance between the maximally responding populations of neurons, which is in line with the observed merging of whisker representations at the level of neuronal spiking (37, 38, 42, 44, 45). We found that increasing the duration of DWE had
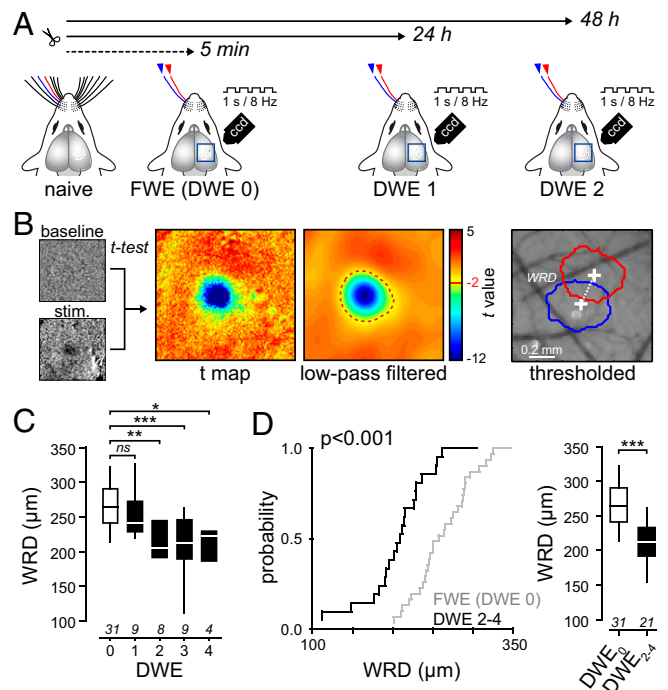

Fig. 1. IOS detects DWE-evoked plasticity of whisker representation in S1. (*A*) Schematic of whisker trimming and IOS recording. (*B*, *Left*) Examples of averaged baseline and stimulus-related raw IOS evoked by one train of whisker deflections. (*Middle*) unfiltered and low-pass-filtered t-value maps computed from 20 stimulations. Only pixels with a t-value lower than −2 are included in the responding area (red dashed line). (*Right*) Whisker C1 (blue) and C2 (red) responding areas. WRD: Euclidian distance between the peaks of the C1 and C2 response areas. (*C*) Median (± interquartile range) WRD as a function of deprivation duration (in days). (*D*, *Left*) Cumulative distribution of WRD in control mice (FWE) and upon DWE. (*Right*) Median (± interquartile range) WRD. Number of recorded mice is indicated below. *$P < 0.05$; **$P < 0.01$; ***$P < 0.001$.

no further effect on the WRD (Fig. 1C), indicating that the merging had reached a maximum within 2 d and remained stable for at least 4 d. Importantly, this shift occurred at a time at which no alterations in the activity of layer 4 granular neurons had been observed (38, 44). This suggests that the changes in IOS observed between 2 and 4 d of DWE (Fig. 1D) depend on experience rather than on alterations in first-order sensory input and are primarily driven by changes of neural activity within L2/3 (44, 46, 47). Hereafter, we will refer to DWE when whiskers were trimmed for 2 to 4 d and to FWE when whiskers were trimmed under anesthesia, just prior to imaging.

DWE Increases NMDAR-Mediated Dendritic Plateau Probabilities and Long-Latency Action Potentials in L2/3 Pyramidal Neurons. Next, we performed whole-cell recordings of L2/3 pyramidal neurons in vivo in the C2 barrel-related column while deflecting either the principal whisker (PW, C2) or surrounding whisker (SW, C1) in FWE and DWE mice (Fig. 2). In accordance with previous reports (12, 48–50), single principal whisker deflections evoked compound postsynaptic potentials (PSPs) that contained short- and long-latency components (Fig. 2 *A* and *B* and *SI Appendix,* Fig. S1). While the former reflect lemniscal inputs, the latter may represent paralemniscal-mediated dendritic NMDAR-mediated potentials that spread toward the soma (36, 51). Short-latency PSPs were reliably evoked in successive trials, with a peak amplitude that was always higher upon PW deflections as compared to SW deflections (PW: 9.95 ± 0.9 mV, $n = 33$; SW: 6.67 ± 0.7 mV, $n = 31$; $P < 0.001$) (*SI Appendix,* Fig. S2). In contrast,
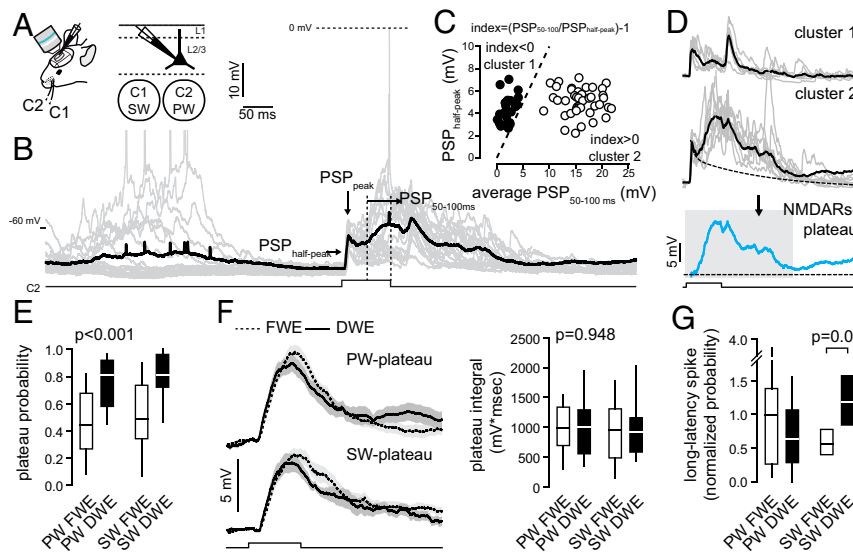
Fig. 2. DWE increases plateau potential probabilities. (*A*) Schematic of recordings in L2/3 cells in vivo in the C2 barrel-related column after >2 d of DWE. (*B*) Single-cell examples of principal (C2) whisker-evoked responses (gray, single trial traces; dark, averaged trace). Square pulse lines, C2 whisker deflection (100 ms). (*C*) For each trial, the relationship between the PSP half-peak amplitude and the average membrane potential between 50 and 100 ms after the onset reveals two distinct clusters. Dashed line represents the identity line. (*D*) Cluster 1 is defined by an index <0 and consists of PSPs containing only a short-latency component that quickly returns to the resting membrane potential. Cluster 2 is defined by an index >0 and consists of compound PSPs with both short- and long-latency components. The long-latency component of the PSP depends on NMDAR (36). For each cell, the NMDAR-plateau potential (*Bottom*) is derived by subtracting the mean cluster 1 response from the mean cluster 2 response. The integral of the plateau potential is measured from 0 to 300 ms (gray box). (*E*) Median ($\pm$ interquartile range) plateau potential probability. (*F*, *Left*) Plateau potential grand average (all recorded cells averaged) $\pm$ SEM, evoked by the PW (*Top*) and SW (*Bottom*) in control mice (dotted line, FWE) and upon DWE (solid line). Square pulse lines, whisker deflection (100 ms). (*Right*) Median ($\pm$ interquartile range) plateau potential integral. (*G*) Mean ($\pm$ interquartile range) long-latency spike probability (normalized to the spiking probability measured in control mice upon PW stimulation). For *E*–*G*, PW and SW correspond to C2 and C1 whiskers, respectively.

long-latency PSPs occurred with variable probabilities (Fig. 2*B*). We extracted these long-latency PSPs as previously described (36). Briefly, for each whisker deflection, the relationship between the PSP half-peak amplitude and the average membrane potential between 50 and 100 ms after the onset reveals two distinct clusters of sensory-evoked PSPs (Fig. 2 *B* and *C* and *SI Appendix,* Fig. S1 *A–C*). Cluster 1 was defined by an index <0, which consisted of short-latency PSPs that quickly returned to the resting membrane potential. Cluster 2 was defined by an index >0 (Fig. 2*C*), which consisted of compound PSPs containing both short- and long-latency components. The long-latency component of the PSPs in cluster 2 was obtained by subtracting the peak-scaled PSP average of cluster 1 from the PSP average of cluster 2 (Fig. 2*D* and *SI Appendix,* Fig. S1*C*). It was previously shown that these late components disappear when NMDAR conductances are blocked and thus represent dendritic plateau potentials (36). Here, we used three different parameters to quantify NMDAR-mediated plateau potentials: the probability of a whisker response to include a long-latency depolarization (cluster 2), the integral of the long-latency depolarization of the traces in cluster 2, and the strength of the long-latency depolarization (the latter being the product of the integral and probability) (*SI Appendix,* Fig. S1 *C* and *F*).

We first compared the probability of the extracted NMDAR-mediated plateaus as elicited by the PW and the SW between FWE and DWE mice. In FWE mice, the PW and SW evoked plateau potentials with similar probabilities (PW: 0.47 ± 0.04, $n = 33$; SW: 0.51 ± 0.05, $n = 31$; $P = 0.305$; Fig. 2*E*). The integral of the plateau potentials was also similar (PW: 985 ± 87 mV*msec, $n = 33$; SW: 951 ± 108 mV*msec, $n = 31$; $P = 0.396$; Fig. 2*F*). Together, this confirms that NMDAR-mediated plateau potentials, in contrast to short-latency AMPAR-mediated PSPs, are not whisker-selective (36). DWE significantly increased the mean probability of both the PW- and SW-evoked

plateau potentials (FWE, PW: 0.47 ± 0.04, $n = 33$; SW: 0.51 ± 0.05, $n = 31$; DWE, PW: 0.762 ± 0.04, $n = 20$; SW: 0.786 ± 0.05; $n = 20$; $P < 0.001$) (Fig. 2*E*), but did not change the plateau-potential integrals ($P = 0.948$) (Fig. 2*F* and *SI Appendix,* Fig. S1*F*) nor the short-latency PSPs (*SI Appendix,* Fig. S2). However, DWE did increase the SW/PW ratio of short-latency peak amplitudes, confirming that this paradigm causes a relative strengthening of SW-associated inputs (12, 37, 38, 44) (*SI Appendix,* Fig. S2). The plateau potentials occasionally elicited action potentials. These were triggered with long delays after the whisker stimulus (Fig. 2*B* and *SI Appendix,* Fig. S1 *D* and *E*), which is consistent with the earlier finding that long-latency spikes in the barrel cortex may depend on NMDARs (48, 52). In line with the increased probability of evoked plateau potentials, DWE also increased the probability of SW-evoked long-latency spikes (Fig. 2*G* and *SI Appendix,* Fig. S1 *D–F*). PW-evoked long-latency action potentials were not increased, which may be related to the higher propensity for the PW to evoke short-latency spikes rather than long-latency spikes (*SI Appendix,* Fig. S1 *D–F*) (12). Collectively, these data indicate that DWE concomitantly increases the probability of whisker-evoked NMDAR-mediated plateau potentials and SW-evoked long-latency spikes in L2/3 pyramidal neurons and merges the cortical representation of the two spared whiskers.

Increased NMDAR-Mediated Plateau Potential Probabilities Depend on Paralemniscal Synaptic Input. In naive mice, NMDAR-mediated plateau potentials in L2/3 pyramidal neurons depend on paralemniscal synaptic inputs from the POm of the thalamus (36). Here, we hypothesized that the increase in plateau potentials upon DWE is both NMDAR and POm-dependent. First, we confirmed that the plateau potential probability decreased in the presence of the NMDAR open-channel blocker MK-801 (1 mM) inside the intracellular solution (iMK801; DWE/control: 0.762 ± 0.04,

Pagès et al.
An increase in dendritic plateau potentials is associated with experience-dependent cortical map reorganization

PNAS | 3 of 8
https://doi.org/10.1073/pnas.2024920118

www.manaraa.com

$n = 20$; DWE/+iMK801: 0.2 ± 0.07, $n = 7$; $P < 0.001$) (Fig. 3 *B–D*). A local injection of the GABA-A receptor (GABA-AR) selective agonist muscimol into the POm also reduced the probability of plateau potentials (Fig. 3 *B–D*). This did not occur when the injections omitted the POm (DWE/muscimol in the POm: 0.14 ± 0.04, $n = 6$; DWE/muscimol omitting POm: 0.7 ± 0.04, $n = 6$; $P < 0.001$) (Fig. 3 *B–D*). In accordance with the probability, the plateau strength (the product of the probability and the integral) also significantly decreased when NMDARs or the activity of the POm was blocked (Fig. 3 *E* and *F*), while leaving the integrals of the remaining plateau potentials unaffected (*SI Appendix*, Fig. S2C). These data indicate that the DWE-associated plateau potentials in L2/3 neurons are mediated by NMDARs and are dependent on POm afferents.

GABA-AR–mediated inhibition in the barrel cortex shunts excitatory conductances in pyramidal distal dendrites and spines (53–56) and impairs NMDAR-dependent synaptic plasticity (12, 34). Thus, inhibitory inputs may gate whisker-evoked NMDAR-mediated plateau potentials (56). To test this, we added the GABA-AR antagonist picrotoxin to the intracellular recording solution (iPTX, 1 mM), which has been shown to efficiently suppress whisker-evoked inhibition in pyramidal neurons, probably through the small and local diffusion of the drug in and around the recorded neuron (12, 57). The GABA-AR block increased the probability of plateau potentials in FWE mice (absolute values; FWE/control: 0.46 ± 0.04, $n = 33$; FWE/

+iPTX: 0.67 ± 0.09, $n = 6$; $P = 0.03$) (Fig. 3D and *SI Appendix*, Fig. S3). Importantly, the probability increased to a level that was similar to DWE mice (absolute values; DWE/control: 0.762 ± 0.04, $n = 20$; FWE/+iPTX: 0.67 ± 0.09, $n = 6$; $P = 0.4$) (Fig. 3D). Similar results were obtained when plateau potential strength was considered (Fig. 3 *E* and *F*), suggesting that GABA-AR inhibition is involved in the gating of the POm-dependent and NMDAR-mediated plateau potentials. To test whether the increase of plateau potential probability was indeed related to reduced inhibition, we extracted the plateau potentials after DWE in presence of PTX in the intracellular solution (Fig. 3 *D–F* and *SI Appendix*, Fig. S3). We found that DWE occluded the effect of the GABA-AR block; i.e., iPTX increased plateau potentials to the same extent in DWE as in FWE mice (Fig. 3 *D–F* and *SI Appendix*, Fig. S3). Altogether, our results indicate that the DWE-evoked increase in plateau potential probabilities depends on NMDAR conductance and paralemniscal afferents, possibly facilitated by disinhibition.

Relationship between Whisker-Evoked Plateau Potentials and Functional Map Reorganization. In FWE mice, the PW and SW drove plateau potentials with similar probabilities (Fig. 2E), suggesting that they are whisker nonspecific. The plateau potential occurrence probabilities were enhanced upon DWE (Fig. 2E), which increased the long-latency spiking rate for SW deflections (Fig. 2G). In addition, 8-Hz trains of single whisker deflections evoked sustained depolarizations that increased upon DWE (*SI Appendix*, Fig. S4). Together, this suggests that the decrease in WRD as seen in IOS imaging (Fig. 1) depends on plateau-potential–mediated mechanisms. To further explore the relationship between plateau potentials and the merging of whisker representations, we first measured the grand average plateau potential strength for the PW and SW in DWE and FWE mice. DWE increased the PW-evoked plateau strength by 55% (FWE: 0.51 ± 0.07, $n = 33$; DWE: 0.87 ± 0.17, $n = 20$; $P = 0.047$), but the 45% strength increase for SW stimulations did not reach significance (FWE: 0.56 ± 0.09, $n = 31$; DWE: 0.81 ± 0.13, $n = 20$; $P = 0.088$) (Fig. 4). Then we expressed the strength of PW- and SW-evoked plateau potentials as a function of the distance between the spared whisker-evoked IOS centers in DWE mice (Fig. 4C). We observed that, for each of the two spared whiskers, the level of plateau strength negatively correlated with the WRD (PW, $r^2 = 0.47$, $P < 0.01$; SW, $r^2 = 0.75$, $P < 0.001$). We calculated the WRD λ that corresponds to 37% (1/e) of the average of plateau strength maximums (Fig. 4C). Compared to FWE mice, both PW and SW deflections induced stronger plateau potentials in DWE mice with a WRD smaller than λ (PW FWE: 0.51 ± 0.07, $n = 33$; PW DWE: 1.3 ± 0.3, $n = 9$; $P = 0.007$; SW FWE: 0.56 ± 0.09, $n = 31$; SW DWE: 1.07 ± 0.25, $n = 9$; $P = 0.033$). In contrast, we found weaker or no correlation between WRD and the whisker-evoked short-latency peak amplitudes (*SI Appendix*, Fig. S2 *E* and *F*). This indicates that, whereas short-latency lemniscal inputs are unlikely to contribute to the decrease in WRD, the merging of the spared whisker representations is tightly coupled to the paralemniscal-driven plateau strength (Fig. 4C).

We then measured the WRD for the two spared whiskers upon DWE before and after the topical application of the NMDAR antagonists dAP5 or 3-(2-Carboxypiperazin-4-yl)propyl-1-phosphonic acid (CPP) ($n = 4$ and 2 mice, respectively, pooled together) or saline for control (Fig. 4 *D* and *E*). Whereas the WRD remained unchanged upon an injection of saline (normalized WRD; saline–: 1.02 ± 0.16, saline+: 0.97 ± 0.13 μm, $n = 5$; $P = 0.398$; ΔWRD: $-5 \pm 5\%$), it significantly increased upon the pharmacological suppression of the NMDAR conductance in DWE mice (dAP5/CPP–: 0.99 ± 0.12, dAP5/CPP+: 1.4 ± 0.08, $n = 6$; $P = 0.031$; ΔWRD: $40 \pm 14\%$) (Fig. 4 *E* and *F*). Importantly, upon application of dAP5, the distances between
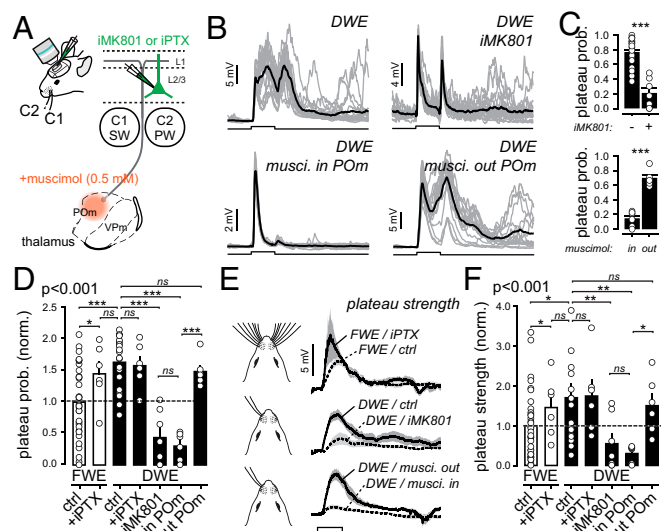

Fig. 3. DWE increases the probability of POm-dependent, NMDAR-mediated plateau potentials. (*A*) Schematic of the thalamo-cortical circuit and pharmacological experiments. Fluorescent muscimol (0.5 mM) is injected locally in the POm ("musci. in POm") or in structures not directly involved in somatosensation ("musci. out POm") for controls. The GABA-A receptor antagonist picrotoxin (iPTX, 1 mM) or the NMDAR open-channel blocker MK-801 (iMK801, 1 mM) are applied directly to the intracellular recording solution. (*B*) Single-cell example of whisker-evoked responses in different conditions. Gray lines, individual trials; black lines, averaged traces. Square pulse lines: C2 whisker deflection (100 ms). (*C*) Mean (±SEM) plateau potential probability after DWE. Circles, individual cells. (*D*) Mean (±SEM) plateau potentials in FWE and DWE mice under different pharmacological conditions. Square pulse lines: C2 whisker deflection (100 ms). (*E*) Grand average of all extracted PW-evoked plateau potential traces (±SEM) in FWE and DWE mice under various pharmacological conditions. Note that, before averaging cells, the mean plateau potential for each cell was multiplied by its probability of occurrence to compute a trace representing the plateau strength (see *SI Appendix*, Fig. S1C for details). (*F*) Mean (±SEM) plateau potential strength in control (FWE) and after DWE under various pharmacological conditions, normalized to the mean measured in FWE mice (dashed line). *$P < 0.05$; **$P < 0.01$; ***$P < 0.001$. ns, not significant.
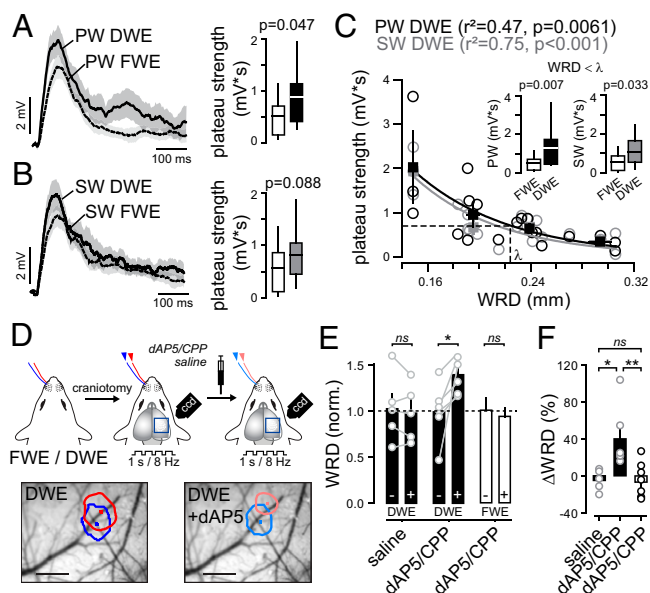
Fig. 4. Blocking NMDAR-mediated plateau potentials restores the IOS map. (*A*, *Left*) Grand average of all extracted PW-evoked plateau potential traces (±SEM) in FWE and DWE mice. Note that, before averaging cells, the mean plateau potential for each cell was multiplied by its probability of occurrence to compute a trace representing the plateau strength. (*Right*) Median (± interquartile range) plateau potential strength. (*B*) Same presentation as in *A* but for SW-evoked plateau strength. (*C*) Relation between WRD and PW (black) and SW (gray) plateau strength. Circles: individual cells; squares: averages. (*Inset*) Median (± interquartile range) plateau potential strength for WRD < λ, in control naive mice (white) and after DWE (black, PW; gray, SW). (*D*) Schematic of experimental protocol with an example of the IOS in a DWE mouse before and after application of dAP5. Scale bar, 500 μm. (*E*) Mean (±SEM) WRD in FWE mice (white bars) after DWE (black bars) under different pharmacological conditions (±: before/after drug application, respectively). (*F*) ΔWRD in FWE mice (white bar) and DWE mice (black bars) following saline or dAP5 application. Blocking NMDAR conductance with dAP5 significantly increases the WRD only in DWE mice. *$P < 0.05$; **$P < 0.01$.

the whisker-evoked IOS areas remained unchanged in control FWE mice (dAP5/CPP−: 1 ± 0.12, dAP5/CPP+: 0.93 ± 0.09, $n = 7$; $P = 0.445$; ΔWRD: −6 ± 8%) (Fig. 4 *E* and *F*). Altogether, these results suggest that the increase in the NMDAR-mediated plateau potential strength participates in the DWE-evoked fusion of spared whisker representations in S1.

Discussion

We used a DWE paradigm in mice to investigate mechanisms of cortical map plasticity in S1. In this paradigm, the trimming of all but two adjacent whiskers causes the spared whiskers to increase their excitatory drive of neurons in the neighboring spared barrel column but not in the deprived areas (37, 38, 44). This plasticity is more modest as compared to a single-whisker experience paradigm, in which the expansion of the spared whisker representation extends far into deprived cortical areas (2, 46). Imaging of intrinsic optical signals, which has been described to correlate with sensory-evoked spiking on an ~100-μm spatial scale (58), readily captures single-whisker map plasticity (41). Using IOS imaging, we found that the distance between the centers of the spared whisker's cortical representations narrows significantly (Fig. 1). This recapitulates the results of extracellular recordings in that it detects the mutual expansion of spared surround whisker-evoked neuronal population activity in both spared barrel columns (2, 4). Thus, our data confirm that IOS imaging has sufficient resolution to visualize even subtle forms of map plasticity such as found under anesthesia upon DWE (9).

Whisker map changes upon DWE are thought to be driven primarily by modulated activity of L2/3 and governed by Hebbian forms of plasticity (37, 38, 44). Remarkably, only a small fraction of L2/3 pyramidal neurons in S1 discharges action potentials in response to a single-whisker deflection (59). This implies that the map changes as observed using IOS imaging are constituted by alterations in a sparsely spiking population of neurons. We found that DWE not only changes the ratios of PW- and SW-driven short-latency PSP (*SI Appendix*, Fig. S2), but also promotes the generation of SW-driven long-latency spikes (Fig. 2) (48). Since IOS integrates activity over relatively long time spans, these long-latency spikes could have contributed to the reduced distance between the spared whisker representations. This possibility is corroborated by the observation that a train of whisker deflections similar to the one used for IOS imaging evokes plateau potentials (36), which are enhanced upon DWE (*SI Appendix*, Fig. S4). Moreover, a block of NMDARs after DWE decreased plateau potential probabilities and restored the distance between neighboring spared whisker-evoked IOS (Figs. 3 and 4). Together, this suggests that the increase in plateau potentials and the associated long-latency spikes contribute to changes in the IOS map. It is also tempting to speculate that the IOS map changes not only depend on somatic short and long-latency spikes, but also are directly generated by the subthreshold plateau potentials, which are driven by local active mechanisms in apical dendrites and are accompanied by substantial ion flux (36, 51, 60–62). Since IOS may strongly depend on ion-related water movements (63), such strong ion fluxes could have contributed to the DWE-evoked map changes in our experiments.

Multiple mechanisms could explain the increase in whisker-evoked plateau potentials. Here (Fig. 3), as in previous work (36), we show that plateau potentials in the barrel cortex depend in part on activity of the POm division of the thalamus. POm neurons send dense axonal projections to L1 in S1 (23, 29), where they spread out over multiple barrel columns and make synaptic contacts with apical dendrites of numerous L2/3 pyramidal neurons (22, 28–30, 32, 35, 36, 64, 65). Interestingly, neurons located in this higher-order thalamic nucleus have large receptive fields (26, 30, 66), and the POm input-recipient L2/3 neurons are characterized by large- and short-latency responses to multiple whisker deflections (30). Thus, the increase in plateau potentials upon DWE could point to an increased activity of POm neurons projecting to L1. POm neurons receive powerful inhibitory inputs from the zona incerta (ZI) (67, 68), which might in turn affect the function and activity of POm depending on the strength of this inhibition, notably during pathological conditions (69). In addition, the ZI-POm connections are strongly modulated by the release of neuromodulators such as acetylcholine, raising the possibility that POm activity could be strongly gated by arousal (70, 71).

Another mechanism for the increase in plateau potentials may include the additional cholinergic effects on dendritic computational properties. Acetylcholine promotes the generation of long-lasting dendritic plateau potentials (72) that could eventually facilitate the plasticity of TC projections (73). On the other hand, accumulating evidence suggests that plateau potentials are strongly and specifically controlled by dendrite-targeted inhibition (56, 74). Here, we found that locally blocking GABA-AR–mediated inhibition dramatically increased the occurrence of whisker-evoked plateau potentials. This occurred in both naive and deprived mice to a similar extent (*SI Appendix*, Fig. S3). Mechanistically, this modulation of dendritic excitability could be driven by the inhibition of interneurons that specifically shunt synaptic inputs from TC projections (53, 75) and/or by the stimulation of TC-mediated disinhibitory motifs (20, 34). In line with these possibilities, it is becoming increasingly clear that

Pagès et al.
An increase in dendritic plateau potentials is associated with experience-dependent cortical map reorganization

PNAS | 5 of 8
https://doi.org/10.1073/pnas.2024920118

sensory map plasticity depends on intricate changes in inhibitory and disinhibitory circuits (1, 8, 9, 12).

What could be the consequences of the increase in dendritic plateau potentials upon alterations of sensory experience? Previous work shows that plateau potentials are strong drivers of synaptic LTP (36, 76, 77), which is intimately associated with map plasticity in the barrel cortex (2, 4, 78). Moreover, TC inputs from POm can also drive cortical LTP through disinhibition (34). Thus, upon DWE, an increase of POm-originating inputs or activity thereof might facilitate LTP in L2/3 pyramidal neurons by evoking disinhibition and plateau potentials, both of which generate favorable conditions for the integration, stabilization, and strengthening of relevant synaptic inputs (79). Interestingly, only pyramidal neurons located in the supragranular (L2/3) and infragranular (L5) layers of the spared barrels, but not in L4, rapidly increase their activity in response to changes in sensory experience (38, 44). This observation has led to the hypothesis that, in adult animals, plasticity occurs first in L2/3 and L5 (4). Interestingly, DWE disproportionally reduces the SW-associated inhibitory inputs on L2/3 pyramidal cells, which in turn facilitates the induction of LTP by surround inputs (12). Thus, it is conceivable that L2/3 and L5 pyramidal neurons rapidly respond to DWE by a combination of whisker-nonspecific POm input and disinhibition, resulting in increased plateau potentials which subsequently may lead to elevated levels of synaptic plasticity (*SI Appendix*, Fig. S5).

Functional studies in vivo have highlighted the pivotal role of dendritic nonlinear events in sensory-evoked spiking and plasticity (36, 51, 80, 81), as well as the control of active behavior and perceptual discrimination (82, 83). It will be interesting in future studies to dissect the relationship between higher-order thalamic inputs to the cortex and experience-dependent synaptic and map plasticity.

Materials and Methods

Ethical Authorization and Whisker Deprivation. All experiments were performed in accordance with the *Guide for the Care and Use of Laboratory Animals* (84) and the European Communities Council Directive of September 22, 2010 (2010/63/EU, 74), as well as the Federal Food Safety and Veterinary Office of Switzerland and in agreement with the veterinary office of the Canton of Geneva (license numbers 1007/3668/2, GE/28/14, GE/61/17, and GE/74/18). Experimental protocols were approved by the institutional ethical committee guidelines for animal research (Comité d'éthique de Bordeaux, no. 50DIR_15-A) and by the French Ministry of Research (agreement no.18892).

We used male C57BL6/J 5- and 6-wk-old mice from Charles River Laboratories that were housed with littermates (three mice per cage) in a 12-h light–dark cycle. Cages were enriched with tunnels. Food and water were provided ad libitum. Mice were separated into two groups. One group was exposed to a brief period of DWE (1 to 4 d: DWE_1, DWE_2, DWE_3, DWE_4) by clipping all whiskers except C1 and C2, while, for the control group, all whiskers were left intact to allow FWE. To facilitate the identification of the C1 and C2 whiskers, all whiskers of FWE mice except the C1 and C2 whiskers were also trimmed. However, to exclude an effect of whisker trimming on sensory perception, this was achieved only during anesthesia and for no longer than 5 min before experimental procedures. These mice never experienced DWE during wakefulness. Mice from the FWE group were then allocated to the group of DWE_0.

Intrinsic Optical Imaging. Intrinsic optical signals were obtained through the intact skull using a light guide system with a 700-nm (bandwidth of 20 nm) interference filter and stable 100-W halogen light source, as previously described (43). Briefly, isoflurane (4% with ~0.5 L/min O_2) combined with an intraperitoneal (i.p.) injection of urethane (1.5 g/kg in lactated ringer solution containing in [mM] 102 NaCl, 28 Na L lactate, 4 KCl, 1.5 $CaCl_2$) was used to induce anesthesia that was prolonged by supplementary urethane (0.15 $g \cdot kg^{-1}$) if necessary. To prevent risks of inflammation, brain swelling, and salivary excretions, 40 μL of dexamethasone (Dexadreson, 0.1 mg/mL, intramuscularly) and glycopyrrolate (Robinul-V, 0.01 mg/kg, subcutaneously) was injected before the surgery. Adequate anesthesia (absence of toe pinch and corneal reflexes and vibrissae movements) was constantly checked and

body temperature was maintained at 37 °C using a heating-pad positioned underneath the animal. Ophthalmic gel was applied to prevent eye dehydration. Analgesia was provided as described for viral injection (with lidocaine and buprenorphine). After disinfection of the skin (with modified ethanol 70% and betadine), the skull was exposed, and an ~3-mm plastic chamber was attached to it above the prefrontal cortex using a combination of super glue (Loctite) and dental acrylic and dental cement (Jet Repair Acrylic, Lang Dental Manufacturing).

The head of the animal was stabilized using a small stereotaxic frame, and the body temperature was kept constant with a heating pad. An image of the surface vascular pattern was taken using a green light (546-nm interference filter) at the end of each imaging session. Images were acquired using the Imager 3001F (Optical Imaging) equipped with a large spatial 602×804 array, fast readout, and low read noise charge-coupled device (CCD) camera. The size of the imaged area was adjusted by using a combination of two lenses with different focal distances (upper lens: Nikon 135 mm, f2.0; bottom lens: Nikon 50 mm, f1.2). The CCD camera was focused on a plane 300 μm below the skull surface. Images were recorded at 10 Hz for 5 s with a spatial resolution of 4.65 μm/pixel comprising a total area of 2.9×3.7 mm². Whisker C2 was deflected back and forth (20 stimulations at 8 Hz for 1 s) using a glass capillary attached to a piezoelectric actuator (PL-140.11 bender controlled by an E-650 driver; Physik Instrumente) triggered by a pulse stimulator (Master-8, A.M.P.I.). Each trial consisted of a 1-s baseline period (frames 1 to 10), followed by a response period (frames 11 to 20) and a poststimulus period (frames 21 to 50). Intertrial intervals lasted 20 s to avoid contamination of the current intrinsic optical signal by prior stimulus. Intrinsic signals were computed by subtracting each individual frame of the response period by the average baseline signal. The obtained intrinsic signal was overlapped with the vasculature image using ImageJ software (85) to precisely identify the C2 whisker cortical representation.

In Vivo Electrophysiology.

Whole-cell recordings. After intrinsic optical imaging, a small ~1- × 1-mm craniotomy (centered above the C2 whisker maximum intrinsic optical response) was made using a pneumatic dental drill, leaving the dura intact. Whole-cell patch-clamp recordings of L2/3 pyramidal neurons were obtained as previously described (36). Briefly, high positive pressure (200 to 300 mbar) was applied to the pipette (5 to 8 MΩ) to prevent tip occlusion, when passing the pia. Immediately after, the positive pressure was reduced to prevent cortical damage. The pipette resistance was monitored in the conventional voltage clamp configuration during the descendent pathway through the cortex (until –200 μm from the surface) of 1-μm steps. When the pipette resistance abruptly increased, the 3- to 5-GΩ seal was obtained by decreasing the positive pressure. After break-in, membrane potential was measured, and dialysis could occur for at least 5 min before launching the recording protocols. Current-clamp recordings were made using a potassium-based internal solution (in mM: 135 potassium gluconate, 4 KCl, 10 Hepes, 10 Na2–phosphocreatine, 4 Mg-ATP, 0.3 Na–GTP, and 25 μM, pH adjusted to 7.25 with KOH, 285 mOsM) and acquired using a Multiclamp 700B Amplifier (Molecular Devices). A spiking pattern of patched cells was analyzed to identify pyramidal neurons. Offline analysis was performed using custom routines written in Sigmaplot (Systat), IGOR Pro (WaveMetrics), and Matlab (Mathworks).

Whisker-evoked postsynaptic potentials in down state. Whisker-evoked PSPs were evoked by back-and-forth deflection of the whisker (100 ms, 0.133 Hz) using piezoelectric ceramic elements attached to a glass pipette ~4 mm away from the skin. The voltage applied to the ceramic was set to evoke a whisker displacement of ~0.6 mm with a ramp of 7 to 8 ms. The C1 and C2 whiskers were independently deflected by different piezoelectric elements. The amplitudes of the evoked PSPs were more pronounced during down states as opposed to the up states. Therefore, to facilitate comparisons of PSPs under different conditions, analysis was confined to short-latency peak amplitudes (within 40 ms after the stimulus artifact) and integrals (within 100 ms after the stimulus artifact) and only if they arose during membrane potential down states. Peak amplitude and integral analysis were performed on each trace and then presented as a mean of at least 30 whisker-evoked responses. To define up and down states, a membrane potential frequency histogram (1-mV bin width) was computed for each recorded cell. For each trial, the average membrane potential was determined (10 ms before the stimulus artifact), and if it overlapped with the potentials of the second peak, the trace was excluded. Onset latency of PSPs in down state was defined as the time point at which the amplitude exceeded 3× SD of the baseline noise over 5 ms prior to stimulation. It was determined based on an average of at least 20 whisker-evoked PSP traces.

Extraction of long-latency plateau potentials. Long-latency plateau potentials were extracted as previously described (36). Briefly, for each whisker deflection, the relationship between the PSP half-peak amplitude and the average membrane potential between 50 and 100 ms after the onset reveals two distinct clusters of sensory-evoked PSPs. Cluster 1 was defined by an index <0, which consisted of short-latency PSPs that quickly returned to the resting membrane potential. Cluster 2 was defined by an index >0, which consisted of compound PSPs containing both short- and long-latency components. The long-latency component of the PSPs in cluster 2 was obtained by subtracting the peak-scaled PSP average of cluster 1 from the PSP average of cluster 2. It was previously shown that these late components disappear when NMDAR conductances are blocked and thus represent dendritic plateau potentials (36).

We used four parameters to quantify the long-latency components of the whisker responses: their probabilities, their integrals, and their strength (*SI Appendix*, Fig. S1 *A–C* and *F*), as well as the probability for them to evoke spikes (*SI Appendix*, Fig. S1 *D–F*). For each cell and for each whisker, the plateau potentials were inferred by subtracting the mean cluster 1 response (scaled to the mean cluster 2 response) from the mean cluster 2 response. The integral of the extracted plateau was measured from 0 to 300 msec. The probability of plateau potential was obtained by dividing the number of whisker-evoked responses from cluster 2 by the total number of whisker-evoked deflections. The strength of plateau potential was obtained by multiplying the integral and the probability of plateau potentials (*SI Appendix*, Fig. S1*C*). Long-latency spikes were defined as whisker-evoked spikes that occur after the timing (+5 ms) of the short-latency PSP peak (+5 ms; *SI Appendix*, Fig. S1*E*).

Drug application. GABA-A receptors and NMDA receptors were blocked by local and intracellular diffusion of PTX (Sigma, 1 mM) and the NMDA receptor open-channel blocker MK-801 (Tocris, 1 mM) in the recording pipette solution, respectively. The local injection of the fluorescent tag of muscimol was performed as previously described (36). Briefly, mice were anesthetized with isoflurane and urethane as described above, before being fixed in a stereotaxic frame. Analgesia was provided by local application of lidocaine and i.p. injection of buprenorphine. A burr hole was made to inject the fluorescent muscimol Bodipy(R)-TMR(X) (500 μM in cortex buffer with 5% dimethylsulfoxide, Invitrogen) in the POm. The caudal sector of the POm that projects mainly to L1 of S1 (29) was specifically targeted using the following stereotaxic coordinates: rostro-caudal: −2.00 mm; medio-lateral: −1.20 mm; dorso-ventral: −3.00 mm from the bregma. Glass pipettes (Wiretrol, Drummond) were pulled, back-filled with mineral oil, and front-loaded with the muscimol solution. From 100 to 150 nL was delivered (20 nL/min) using an oil hydraulic manipulator system (MMO-220A, Narishige). For control injection, the same volume of the fluorescent muscimol was injected in thalamic structures that are not involved in somatosensory processing. The craniotomy was then covered with Kwik-Cast (WPI), and mice were prepared for intrinsic optical imaging and whole-cell recordings as described above. To achieve a maximal suppression of neuronal activity, patch-clamp recordings were performed at least 1 h after the injection but no longer than 4 h after the injection. After completion of the experiment, mice were transcardially perfused with 4% paraformaldehyde (PFA) in PBS, and their brains were extracted and postfixed in PFA overnight. Coronal brain sections of 100 μm were then made to confirm the site and spread of injections.

For drug application during IOS recordings, DAP5 (0.1 mM) and saline solutions (in mM: 125 NaCl, 5 KCl, 10 glucose, 10 Hepes, 2 CaCl2, and 2 MgSO$_4^-$, pH 7.4) were topically applied to the dura mater through a customized open cranial window. Mice were anesthetized using an i.p. injection of a mixture containing medetomidin (Dorbene, 0.2 mg·kg⁻1), midazolam (Dormicum, 5 mg·kg⁻1) and fentanyl (Duragesic, 0.05 mg·kg⁻1) in sterile NaCl

0.9%. The cortical region containing C1 and C2 representations was placed in the center of the field of view. Both whiskers were mapped under saline conditions first and then after a 15-min bath application of DAP5-containing solution.

Spatiotemporal Analysis of Intrinsic Optical Signal. The intrinsic optical signals were analyzed as previously described (43). The signals were spatially binned (6 × 6, final resolution: 27.9 μm/pixel or 3 × 3, final resolution: 13.95 μm/pixel), and a high-pass filter was then applied by subtracting from each image frame the same image frame that was convolved using a 1,270-μm full-width at half maximum (FWHM) Gaussian kernel. The whisker-evoked intrinsic optical signals were then simulated using a pixel-by-pixel paired *t* test, comparing the baseline period and the response period of all trials within a session. The *t* maps for each individual trial were low-pass-filtered with a 340-μm FWHM Gaussian kernel and averaged into a final *t* map response. A threshold was set to *t* < −2.0, and any signal below this value was considered to belong to the stimulus-evoked response area. If the pixel value was *t* ≥ −2.0, it was considered background noise and discarded for quantification. This usually resulted in an image with a clear minimum, representing the response maximum and the barrel's center of mass. Changes in the intrinsic optical signal pixel area caused by whisker trimming were computed as the ratio between the whisker-evoked intrinsic response of the baseline and DWE sessions. All data analysis was performed using a custom software written in MATLAB (MathWorks).

Quantification and Statistical Analysis. All data generated or analyzed during this study are included in the paper and provided in *SI Appendix*, Table S1. Some of the underlying recordings were obtained in a previous study (12), but reanalyzed to support the current dataset. Data are presented as the median ± interquartile range or mean ± SEM, except where stated differently. All statistics were performed using Matlab (Mathworks) with an α significant level set at 0.05. Normality of all value distributions and the equality of variance between different distributions were first assessed by the Shapiro–Wilk and Levene median tests, respectively. Standard parametric tests were used only when data passed the normality and equal variance tests (*P* > 0.05). Nonparametric tests were used otherwise. Only two-sided tests were used. When applicable, pair-wise multiple post hoc comparisons were done by using the Holm–Sidak method. Randomization and blinding methods were not used. No statistical methods were used to estimate sample size, but β-power values were calculated for parametric tests.

Data Availability. All study data are included in the article and/or supporting information.

1. S. Harding-Forrester, D. E. Feldman, "Somatosensory maps" in *Handbook of Clinical Neurology*, G. Vallar, H. B. Coslett, Eds. (Elsevier B.V., 2018), pp. 73–102.
2. D. E. Feldman, Synaptic mechanisms for plasticity in neocortex. *Annu. Rev. Neurosci.* **32**, 33–55 (2009).
3. K. Fox, Anatomical pathways and molecular mechanisms for plasticity in the barrel cortex. *Neuroscience* **111**, 799–814 (2002).
4. D. E. Feldman, M. Brecht, Map plasticity in somatosensory cortex. *Science* **310**, 810–815 (2005).
5. R. L. Clem, A. Barth, Pathway-specific trafficking of native AMPARs by in vivo experience. *Neuron* **49**, 663–670 (2006).
6. R. L. Clem, T. Celikel, A. L. Barth, Ongoing in vivo experience triggers synaptic metaplasticity in the neocortex. *Science* **319**, 101–104 (2008).
7. G. T. Finnerty, L. S. Roberts, B. W. Connors, Sensory experience modifies the short-term dynamics of neocortical synapses. *Nature* **400**, 367–371 (1999).
8. M. A. Gainey, D. E. Feldman, Multiple shared mechanisms for homeostatic plasticity in rodent somatosensory and visual cortex. *Philos. Trans. R. Soc. Lond. B Biol. Sci.* **372**, 20160157 (2017).
9. L. Li, M. A. Gainey, J. E. Goldbeck, D. E. Feldman, Rapid homeostasis by disinhibition during whisker map plasticity. *Proc. Natl. Acad. Sci. U.S.A.* **111**, 1616–1621 (2014).
10. D. R. C. House, J. Elstrott, E. Koh, J. Chung, D. E. Feldman, Parallel regulation of feedforward inhibition and excitation during whisker map plasticity. *Neuron* **72**, 819–831 (2011).
11. Y. Jiao, C. Zhang, Y. Yanagawa, Q.-Q. Sun, Major effects of sensory experiences on the neocortical inhibitory circuits. *J. Neurosci.* **26**, 8691–8701 (2006).
12. F. Gambino, A. Holtmaat, Spike-timing-dependent potentiation of sensory surround in the somatosensory cortex is facilitated by deprivation-mediated disinhibition. *Neuron* **75**, 490–502 (2012).
13. X. Chen, U. Leischner, N. L. Rochefort, I. Nelken, A. Konnerth, Functional mapping of single spines in cortical neurons in vivo. *Nature* **475**, 501–505 (2011).
14. T. Keck *et al.*, Loss of sensory input causes rapid structural changes of inhibitory neurons in adult mouse visual cortex. *Neuron* **71**, 869–882 (2011).
15. D. van Versendaal *et al.*, Elimination of inhibitory synapses is a major component of adult ocular dominance plasticity. *Neuron* **74**, 374–383 (2012).

Pagès et al.
An increase in dendritic plateau potentials is associated with experience-dependent cortical map reorganization

PNAS | 7 of 8
https://doi.org/10.1073/pnas.2024920118

www.manaraa.com

16. M. Oberlaender, A. Ramirez, R. M. Bruno, Sensory experience restructures thalamo-cortical axons during adulthood. *Neuron* **74**, 648–655 (2012).
17. X. Yu *et al.*, Thalamocortical inputs show post-critical-period plasticity. *Neuron* **74**, 731–742 (2012).
18. V. C. Wimmer, P. J. Broser, T. Kuner, R. M. Bruno, Experience-induced plasticity of thalamocortical axons in both juveniles and adults. *J. Comp. Neurol.* **518**, 4629–4648 (2010).
19. N. Jamann, M. Jordan, M. Engelhardt, Activity-dependent axonal plasticity in sensory systems. *Neuroscience* **368**, 268–282 (2018).
20. N. J. Audette, J. Urban-Ciecko, M. Matsushita, A. L. Barth, POm thalamocortical input drives layer-specific microcircuits in somatosensory cortex. *Cereb. Cortex* **28**, 1312–1328 (2018).
21. K. D. Alloway, Information processing streams in rodent barrel cortex: The differential functions of barrel and septal circuits. *Cereb. Cortex* **18**, 979–989 (2008).
22. D. Feldmeyer, Excitatory neuronal connectivity in the barrel cortex. *Front. Neuroanat.* **6**, 24 (2012).
23. V. C. Wimmer, R. M. Bruno, C. P. J. de Kock, T. Kuner, B. Sakmann, Dimensions of a projection column and architecture of VPM and POm axons in rat vibrissal cortex. *Cereb. Cortex* **20**, 2265–2276 (2010).
24. M. Deschênes, E. Timofeeva, P. Lavallée, C. Dufresne, The vibrissal system as a model of thalamic operations. *Prog. Brain Res.* **149**, 31–40 (2005).
25. S. M. Sherman, Functioning of circuits connecting thalamus and cortex. *Compr. Physiol.* **7**, 713–739 (2017).
26. M. E. Diamond, M. Armstrong-James, M. J. Budway, F. F. Ebner, Somatic sensory responses in the rostral sector of the posterior group (POm) and in the ventral posterior medial nucleus (VPM) of the rat thalamus: Dependence on the barrel field cortex. *J. Comp. Neurol.* **319**, 66–84 (1992).
27. P. Veinante, M. Deschênes, Single- and multi-whisker channels in the ascending projections from the principal trigeminal nucleus in the rat. *J. Neurosci.* **19**, 5085–5095 (1999).
28. E. G. Jones, Cortical and subcortical contributions to activity-dependent plasticity in primate somatosensory cortex. *Annu. Rev. Neurosci.* **23**, 1–37 (2000).
29. S. Ohno *et al.*, A morphological analysis of thalamocortical axon fibers of rat posterior thalamic nuclei: A single neuron tracing study with viral vectors. *Cereb. Cortex* **22**, 2840–2857 (2012).
30. J.-S. Jouhanneau *et al.*, Cortical fosGFP expression reveals broad receptive field excitatory neurons targeted by POm. *Neuron* **84**, 1065–1078 (2014).
31. R. A. Mease, M. Metz, A. Groh, Cortical sensory responses are enhanced by the higher-order thalamus. *Cell Rep.* **14**, 208–215 (2016).
32. L. Petreanu, T. Mao, S. M. Sternson, K. Svoboda, The subcellular organization of neocortical excitatory connections. *Nature* **457**, 1142–1145 (2009).
33. A. N. Viaene, I. Petrof, S. M. Sherman, Properties of the thalamic projection from the posterior medial nucleus to primary and secondary somatosensory cortices in the mouse. *Proc. Natl. Acad. Sci. U.S.A.* **108**, 18156–18161 (2011).
34. L. E. Williams, A. Holtmaat, Higher-order thalamocortical inputs gate synaptic long-term potentiation via disinhibition. *Neuron* **101**, 91–102.e4 (2019).
35. W. Zhang, R. M. Bruno, High-order thalamic inputs to primary somatosensory cortex are stronger and longer lasting than cortical inputs. *eLife* **8**, e44158 (2019).
36. F. Gambino *et al.*, Sensory-evoked LTP driven by dendritic plateau potentials in vivo. *Nature* **515**, 116–119 (2014).
37. M. Armstrong-James, M. E. Diamond, F. F. Ebner, An innocuous bias in whisker use in adult rats modifies receptive fields of barrel cortex neurons. *J. Neurosci.* **14**, 6978–6991 (1994).
38. M. E. Diamond, M. Armstrong-James, F. F. Ebner, Experience-dependent plasticity in adult rat barrel cortex. *Proc. Natl. Acad. Sci. U.S.A.* **90**, 2082–2086 (1993).
39. A. Grinvald, E. Lieke, R. D. Frostig, C. D. Gilbert, T. N. Wiesel, Functional architecture of cortex revealed by optical imaging of intrinsic signals. *Nature* **324**, 361–364 (1986).
40. M. M. B. Cardoso, Y. B. Sirotin, B. Lima, E. Glushenkova, A. Das, The neuroimaging signal is a linear sum of neurally distinct stimulus- and task-related components. *Nat. Neurosci.* **15**, 1298–1306 (2012).
41. D. B. Polley, C. H. Chen-Bee, R. D. Frostig, Two directions of plasticity in the sensory-deprived adult cortex. *Neuron* **24**, 623–637 (1999).
42. P. J. Drew, D. E. Feldman, Intrinsic signal imaging of deprivation-induced contraction of whisker representations in rat somatosensory cortex. *Cereb. Cortex* **19**, 331–348 (2009).
43. V. Schubert, D. Lebrecht, A. Holtmaat, Peripheral deafferentation-driven functional somatosensory map shifts are associated with local, not large-scale dendritic structural plasticity. *J. Neurosci.* **33**, 9474–9487 (2013).
44. M. E. Diamond, W. Huang, F. F. Ebner, Laminar comparison of somatosensory cortical plasticity. *Science* **265**, 1885–1888 (1994).
45. D. J. Wallace, B. Sakmann, Plasticity of representational maps in somatosensory cortex observed by in vivo voltage-sensitive dye imaging. *Cereb. Cortex* **18**, 1361–1373 (2008).
46. S. Glazewski, K. Fox, Time course of experience-dependent synaptic potentiation and depression in barrel cortex of adolescent rats. *J. Neurophysiol.* **75**, 1714–1729 (1996).
47. E. A. Stern, M. Maravall, K. Svoboda, Rapid development and plasticity of layer 2/3 maps in rat barrel cortex in vivo. *Neuron* **31**, 305–315 (2001).
48. M. Armstrong-James, E. Welker, C. A. Callahan, The contribution of NMDA and non-NMDA receptors to fast and slow transmission of sensory information in the rat SI barrel cortex. *J. Neurosci.* **13**, 2149–2160 (1993).
49. C. C. H. Petersen, A. Grinvald, B. Sakmann, Spatiotemporal dynamics of sensory responses in layer 2/3 of rat barrel cortex measured in vivo by voltage-sensitive dye imaging combined with whole-cell voltage recordings and neuron reconstructions. *J. Neurosci.* **23**, 1298–1309 (2003).
50. W. B. Wilent, D. Contreras, Synaptic responses to whisker deflections in rat barrel cortex as a function of cortical layer and stimulus intensity. *J. Neurosci.* **24**, 3985–3998 (2004).
51. L. M. Palmer *et al.*, NMDA spikes enhance action potential generation during sensory input. *Nat. Neurosci.* **17**, 383–390 (2014).
52. T. E. Salt, Mediation of thalamic sensory input by both NMDA receptors and non-NMDA receptors. *Nature* **322**, 263–265 (1986).
53. C. Koch, *Biophysics of Computation: Information Processing in Single Neurons* (Oxford University Press, 1999).
54. M. E. Larkum, J. J. Zhu, B. Sakmann, A new cellular mechanism for coupling inputs arriving at different cortical layers. *Nature* **398**, 338–341 (1999).
55. M. E. Larkum, J. Waters, B. Sakmann, F. Helmchen, Dendritic spikes in apical dendrites of neocortical layer 2/3 pyramidal neurons. *J. Neurosci.* **27**, 8999–9008 (2007).
56. L. Palmer, M. Murayama, M. Larkum, Inhibitory regulation of dendritic activity in vivo. *Front. Neural Circuits* **6**, 26 (2012).
57. Y. Yazaki-Sugiyama, S. Kang, H. Câteau, T. Fukai, T. K. Hensch, Bidirectional plasticity in fast-spiking GABA circuits by visual experience. *Nature* **462**, 218–221 (2009).
58. D. Y. Ts'o, R. D. Frostig, E. E. Lieke, A. Grinvald, Functional organization of primate visual cortex revealed by high resolution optical imaging. *Science* **249**, 417–420 (1990).
59. C. P. J. De Kock, R. M. Bruno, H. Spors, B. Sakmann, Layer- and cell-type-specific suprathreshold stimulus representation in rat primary somatosensory cortex. *J. Physiol.* **581**, 139–154 (2007).
60. G. Major, A. Polsky, W. Denk, J. Schiller, D. W. Tank, Spatiotemporally graded NMDA spike/plateau potentials in basal dendrites of neocortical pyramidal neurons. *J. Neurophysiol.* **99**, 2584–2601 (2008).
61. S. D. Antic, W.-L. Zhou, A. R. Moore, S. M. Short, K. D. Ikonomu, The decade of the dendritic NMDA spike. *J. Neurosci. Res.* **88**, 2991–3001 (2010).
62. M. E. Larkum, T. Nevian, M. Sandler, A. Polsky, J. Schiller, Synaptic integration in Tuft dendrites of layer 5 pyramidal neurons: A new unifying principle. *Science* **325**, 756–760 (2009).
63. R. Vincis, S. Lagier, D. Van De Ville, I. Rodriguez, A. Carleton, Sensory-evoked intrinsic imaging signals in the olfactory bulb are independent of neurovascular coupling. *Cell Rep.* **12**, 313–325 (2015).
64. I. Bureau, F. Von Saint, K. Svoboda, Interdigitated paralemniscal and lemniscal pathways in the mouse barrel cortex. *PLoS Biol.* **4**, e382 (2006).
65. B. S. Sermet *et al.*, Pathway-, layer- and cell-type-specific thalamic input to mouse barrel cortex. *eLife* **8**, e52665 (2019).
66. R. Masri, T. Bezdudnaya, J. C. Trageser, A. Keller, Encoding of stimulus frequency and sensor motion in the posterior medial thalamic nucleus. *J. Neurophysiol.* **100**, 681–689 (2008).
67. P. Lavallée *et al.*, Feedforward inhibitory control of sensory information in higher-order thalamic nuclei. *J. Neurosci.* **25**, 7489–7498 (2005).
68. J. C. Trageser, A. Keller, Reducing the uncertainty: Gating of peripheral inputs by zona incerta. *J. Neurosci.* **24**, 8911–8915 (2004).
69. R. Masri *et al.*, Zona incerta: A role in central pain. *J. Neurophysiol.* **102**, 181–191 (2009).
70. R. Masri, J. C. Trageser, T. Bezdudnaya, Y. Li, A. Keller, Cholinergic regulation of the posterior medial thalamic nucleus. *J. Neurophysiol.* **96**, 2265–2273 (2006).
71. J. C. Trageser *et al.*, State-dependent gating of sensory inputs by zona incerta. *J. Neurophysiol.* **96**, 1456–1463 (2006).
72. S. R. Williams, L. N. Fletcher, A dendritic substrate for the cholinergic control of neocortical output neurons. *Neuron* **101**, 486–499.e4 (2019).
73. H. C. Dringenberg, B. Hamze, A. Wilson, W. Speechley, M.-C. Kuo, Heterosynaptic facilitation of in vivo thalamocortical long-term potentiation in the adult rat visual cortex by acetylcholine. *Cereb. Cortex* **17**, 839–848 (2007).
74. M. Larkum, A cellular mechanism for cortical associations: An organizing principle for the cerebral cortex. *Trends Neurosci.* **36**, 141–151 (2013).
75. Y. Kubota, S. Hatada, S. Kondo, F. Karube, Y. Kawaguchi, Neocortical inhibitory terminals innervate dendritic spines targeted by thalamocortical afferents. *J. Neurosci.* **27**, 1139–1150 (2007).
76. F. Brandalise, S. Carta, F. Helmchen, J. Lisman, U. Gerber, Dendritic NMDA spikes are necessary for timing-dependent associative LTP in CA3 pyramidal cells. *Nat. Commun.* **7**, 13480 (2016).
77. N. L. Golding, N. P. Staff, N. Spruston, Dendritic spikes as a mechanism for cooperative long-term potentiation. *Nature* **418**, 326–331 (2002).
78. S. Glazewski, K. P. Giese, A. Silva, K. Fox, The role of α-CaMKII autophosphorylation in neocortical experience-dependent plasticity. *Nat. Neurosci.* **3**, 911–918 (2000).
79. A. Holtmaat, P. Caroni, Functional and structural underpinnings of neuronal assembly formation in learning. *Nat. Neurosci.* **19**, 1553–1562 (2016).
80. K. Du *et al.*, Cell-type-specific inhibition of the dendritic plateau potential in striatal spiny projection neurons. *Proc. Natl. Acad. Sci. U.S.A.* **114**, E7612–E7621 (2017).
81. J. Cichon, W.-B. Gan, Branch-specific dendritic Ca(2+) spikes cause persistent synaptic plasticity. *Nature* **520**, 180–185 (2015).
82. N. Takahashi, T. G. Oertner, P. Hegemann, M. E. Larkum, Active cortical dendrites modulate perception. *Science* **354**, 1587–1590 (2016).
83. N. L. Xu *et al.*, Nonlinear dendritic integration of sensory and motor input during an active sensing task. *Nature* **492**, 247–251 (2012).
84. National Research Council, *Guide for the Care and Use of Laboratory Animals* (National Academies Press, Washington, DC, ed. 8, 2011).
85. C. A. Schneider, W. S. Rasband, K. W. Eliceiri, NIH image to imageJ: 25 years of image analysis. *Nat. Methods* **9**, 671–675 (2012).

8 of 8 | PNAS
https://doi.org/10.1073/pnas.2024920118

Pagès et al.
An increase in dendritic plateau potentials is associated with experience-dependent